Towards fast and reliable estimations of 3D pressure, velocity and wall shear stress in aortic blood flow

CFD-based machine learning approach

Lin, Daiqi; Kenjereš, Saša

DOI
10.1016/j.compbiomed.2025.110137

Publication date
2025

Document Version
Final published version

Published in
Computers in Biology and Medicine

Computers in Biology and Medicine 191 (2025) 110137

Contents lists available at ScienceDirect

Computers in Biology and Medicine

journal homepage: www.elsevier.com/locate/compbiomed

Towards fast and reliable estimations of 3D pressure, velocity and wall shear stress in aortic blood flow: CFD-based machine learning approach

Daiqi Lin, Saša Kenjereš *

Department of Chemical Engineering, Faculty of Applied Sciences, Delft University of Technology, Van der Maasweg 9, 2629 HZ Delft, The Netherlands
J.M. Burgerscentrum Research School for Fluid Mechanics, Mekelweg 2, 2628 CD Delft, The Netherlands

ARTICLE INFO

Keywords:
Aortic blood flow
CFD
Machine learning
Wall shear stress
Pressure

ABSTRACT

In this work, we developed deep neural networks for the fast and comprehensive estimation of the most salient features of aortic blood flow. These features include velocity magnitude and direction, 3D pressure, and wall shear stress. Starting from 40 subject-specific aortic geometries obtained from 4D Flow MRI, we applied statistical shape modeling to generate 1,000 synthetic aorta geometries. Complete computational fluid dynamics (CFD) simulations of these geometries were performed to obtain ground-truth values. We then trained deep neural networks for each characteristic flow feature using 900 randomly selected aorta geometries. Testing on remaining 100 geometries resulted in average errors of 3.11% for velocity and 4.48% for pressure. For wall shear stress predictions, we applied two approaches: (i) directly derived from the neural network-predicted velocity, and, (ii) predicted from a separate neural network. Both approaches yielded similar accuracy, with average error of 4.8 and 4.7% compared to complete 3D CFD results, respectively. We recommend the second approach for potential clinical use due to its significantly simplified workflow. In conclusion, this proof-of-concept analysis demonstrates the numerical robustness, rapid calculation speed (less than seconds), and good accuracy of the CFD-based machine learning approach in predicting velocity, pressure, and wall shear stress distributions in subject-specific aortic flows.

1. Introduction

Aortic pathologies are closely related to aberrant blood flow patterns and hemodynamic metrics, such as wall shear stress (WSS) [1–3]. Computational Fluid Dynamics (CFD) offers the potential to simulate the aortic blood flow in great detail. To perform patient-specific hemodynamic simulations, researchers need to utilize both the geometry of blood vessels (e.g. obtained from magnetic resonance imaging (MRI) [4], ultrasound (US) [5] or computed tomography (CT) [6] scans), and measured blood flow rates (e.g. from 4D Flow MRI or US). These investigations have resulted in reporting on clinically relevant hemodynamic metrics, including wall shear stress (WSS) and oscillatory shear index (OSI) [7–9]. CFD offers several advantages over pure imaging clinical studies in analyzing blood flow in aortas, primarily due to its significantly higher spatial and temporal resolution [10]. These advantages include: (i) enhanced visualization of complex flow patterns, (ii) accurate quantification of hemodynamic parameters (e.g. WSS, OSI), (iii) ability to capture inherently transient flow phenomena throughout the cardiac cycle. Moreover, CFD simulations enable modeling of various treatment scenarios and surgical interventions before they are performed, which can be particularly valuable for complex cases of aortic aneurysm, coarctation or dissection. These predictive simulations can aid in treatment planning and optimization, potentially improving patient outcomes [11].

Another advantage of CFD is the availability of diverse physical models for hemodynamics simulation in modern CFD packages. These include advanced fluid–structure interactions (FSI), moving meshes, advanced turbulence models, multi-phase and non-Newtonian fluid models, which enhance the accuracy of blood flow simulations. Furthermore, the field of cardiovascular biomechanics benefits from a strong culture of collaboration and sharing [12]. This has led to the development of high-quality open science resources including: (1) image processing software: ITK-SNAP [13], 3D Slicer [14], VMTK [15], ITK [16]; (2) CFD packages: SimVascular [17], OpenFOAM [18]; (3) open data repositories: PhysioNet [19], Physiome Project [20]. These resources significantly contribute to the advancement of cardiovascular biomechanics simulations and facilitate the wider adoption of CFD techniques in clinical applications.

Despite the significant advantages of CFD and related open sci-

* Corresponding author at: Department of Chemical Engineering, Faculty of Applied Sciences, Delft University of Technology, Van der Maasweg 9, 2629 HZ Delft, The Netherlands.
E-mail addresses: d.l.lin@tudelft.nl (D. Lin), s.kenjeres@tudelft.nl (S. Kenjereš).

https://doi.org/10.1016/j.compbiomed.2025.110137
Received 21 October 2024; Received in revised form 23 March 2025; Accepted 2 April 2025
Available online 18 April 2025

ence environments, its application in clinical diagnosis and treatment remains limited at present [21]. Several technical challenges contribute to this limitation: (1) relatively advanced technical user expertise required, (2) complex workflow, (3) time-consuming process, (4) computational expenses, etc. However, recent developments in biomedical imaging and computational resources have paved the way for machine learning to address these challenges. Machine learning (ML) techniques have demonstrated great promise in: (1) simplifying CFD workflows, (2) reducing time consumption of conventional CFD methods, and (3) enhancing the accessibility of CFD for clinical applications. These recent advancements suggest a potential shift towards more efficient and user-friendly CFD implementation in clinical settings. Several studies have demonstrated the promising application of machine learning techniques in arterial and aortic blood flow simulations.

Liang et al. [22] conducted a feasibility study using deep neural networks (DNNs) to directly estimate steady-state distributions of pressure and blood velocity in the human thoracic aorta. After training on hemodynamic data from CFD simulations, their DNNs could predict velocity magnitude fields with an average error of 1.96% in about one second, demonstrating potential as a fast and accurate surrogate model.

Morgan et al. [23] presented a novel physics-based machine learning technique to rapidly reconstruct wall shear stress and pressure fields in coronary arteries. Their method combined reduced-order CFD modeling (based on the proper orthogonal decomposition, POD) with machine learning to expedite the reconstruction of 3D pressure and shear stress fields.

Pajaziti et al. [24] developed deep neural networks to rapidly predict 3D pressure and velocity-magnitude in the aorta. Their model was trained on 3000 CFD simulations of synthetically generated 3D aortic shapes. The machine learning approach was able to perform CFD simulations about 4000 times faster than conventional solvers, with average errors of 6.01% for pressure and 3.99% for velocity magnitude compared to traditional CFD. These studies demonstrated how machine learning can significantly reduce computational time while maintaining acceptable accuracy of pressure and velocity magnitude predictions (which was within the 2%–6% error range), addressing key challenges in the clinical applications of CFD.

However, the suitability of machine learning-predicted velocity fields for post-processing and deriving hemodynamic metrics (such as WSS) in aortic blood flows has not been thoroughly tested or reported. To make predicted flow field more comprehensive and clinically useful, future models should aim to: (1) predict pressure, velocity vectors, and velocity magnitude simultaneously, and (2) accurately capture velocity gradients in the relatively thin boundary layer along the aorta. If these criteria are met, velocity fields predicted by CFD-based machine learning could potentially derive reasonable wall shear stress estimates on blood vessel walls. This advancement would significantly enhance the clinical applicability of machine learning-based flow predictions in vascular studies.

In this study, we first applied deep neural networks (DNNs) to predict the aortic velocity field (i.e. the velocity magnitude and direction). To test the predictive ability of this method, the obtained velocity field was used to directly calculate the wall shear stress (WSS). Additionally, a neural network was constructed and trained to predict the WSS. The results obtained from these two approaches were compared and analyzed against the ground-truth computational fluid dynamics (CFD) results. Furthermore, the 3D pressure fields were also predicted by neural networks, and the results were compared with those of previous work of [24]. The complete workflow of the present study is shown in Fig. 1, which integrates: (1) the data-augmented dataset of realistic aorta geometries, (2) detailed CFD simulations, (3) development and training of neural networks for pressure and velocity fields, and finally, (4) the derived and predicted WSS.

The present study contains the following novel elements: (i) Simultaneous predictions of physics-based DNNs for 3D pressure, velocity, and wall shear stress for aortic flows; (ii) Our neural network explicitly incorporates the no-slip condition at the aortic wall, enabling physically accurate and consistent velocity predictions; (iii) We introduce a method to derive wall shear stress directly from the predicted velocity field, complementing neural network predictions; (iv) We present a comprehensive analysis of the relationships between aortic geometries and PCA modes.

2. Methodology

2.1. Aorta geometries

Our analysis begins with a total of 40 subject-specific aorta geometries, segmented from 4D Flow MRI scans as described in previous studies [8,25,26], Fig. A.14. This dataset contains scans from ten subjects, each processed using four different segmentation techniques. The morphometric characteristics and details of the considered aortic geometries are provided in [25]. In the current study, consistent with approaches presented in [8,24], aortic side-branches are excluded from the simulations. To prepare the segmented aortic geometry surfaces for CFD simulations, we undertook several steps including surface smoothing, clipping, centerline extraction, and necessary remeshing. All these processes were performed using the open-source Vascular Modeling Toolkit (VMTK), [15].

2.2. Statistical shape model

To perform data augmentation of aortic geometries (due to the relatively small size of the initial 4D Flow MRI-based dataset), we applied the method proposed in [24] to generate a statistical shape model (SSM) from the aortic geometries data shown in Fig. A.14, using the open-source software Deformetrica 4.0 [27].

The statistical shape model was generated by applying the Large Deformation Diffeomorphic Metric Mapping (LDDMM) approach, as described in [28] (see Fig. 2). In this approach, the aorta wall surface is specified as a surface template, which should be as simple and representative as possible. A volume template is then generated by meshing the surface template with tetrahedral cells and a prismatic boundary layer within the aortic interior. The LDDMM method, based on control points, was used to calculate the non-linear deformation of 3D ambient space for each subject relative to the surface template. We specified deformation using a pair set of control points and momenta vectors, with a total of 150 control points. The deformation for the entire dataset can be described with a matrix $\mathcal{M}[40, 450]$. To reduce the size of the deformation matrix $\mathcal{M}$, we applied Principle Component Analysis (PCA). The results (Fig. B.15) show that the first 19 PCA modes were able to capture 99% of the variance of the matrix $\mathcal{M}$.

After performing PCA, the matrix $\mathcal{M}$ was reduced to dimensions $[40, 19]$. To generate 1000 virtual shapes, synthetic deformation vectors were generated using Gaussian distribution sampling (within 2 standard deviations). Following an inverse PCA operation, we obtained a synthetic deformation matrix with dimensions $[1000, 450]$, which was then reshaped to $[1000, 150, 3]$. Note that the matrix elements of the latter indicate the number of geometries, number of control points, and, 3D momenta (coordinate directions) for the control points, respectively.

The open-source software Deformetrica can utilize this deformation matrix to deform both the surface and volume templates of the aorta, producing 1000 virtual geometries. All of these geometries have an identical number of nodes and cells, ensuring structured mesh correspondence. After performing mesh deformation, all corresponding volume meshes also have generated prismatic layers in the proximity of the aortic wall to properly resolve steep velocity gradients within the boundary layers. The importance of this approach will be elaborated in more detail in Section 4.1.

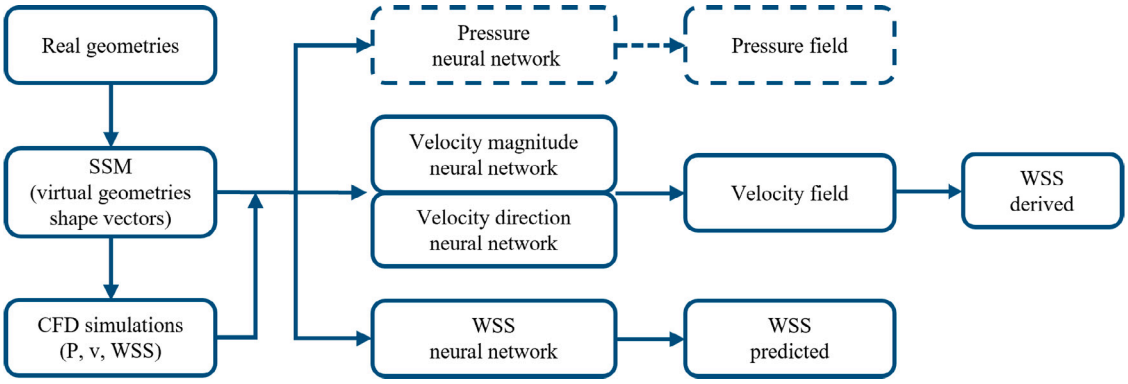

Fig. 1. The workflow adopted in the present study: (i) the data-augmented dataset of realistic aorta geometries, (ii) detailed CFD simulations, (iii) development and training of neural networks for pressure and velocity fields, and finally, (iv) the derived and predicted WSS.

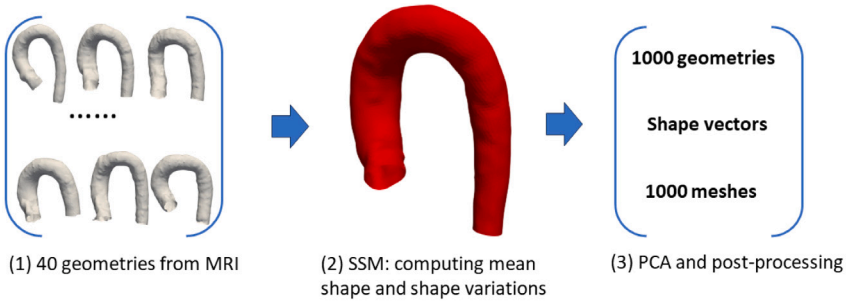

Fig. 2. Workflow of the applied statistical shape model (SSM).

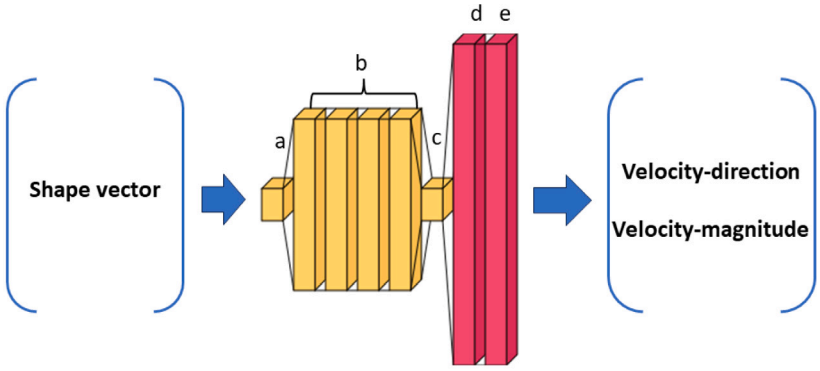

Fig. 3. Structure of neural networks: a,b,c: multilayer perceptron, d: inverse PCA layer, e: no-slip condition layer. Two separate neural networks were built for velocity field prediction.

2.3. Computational fluid dynamics modeling

The steady-state blood flow is governed by the conservation of mass and momentum equations for the incompressible fluid [8], which are written as:

$$\nabla \cdot \mathbf{u} = 0 \tag{1}$$

$$\rho \mathbf{u} \cdot \nabla \mathbf{u} = -\nabla p + \mu \nabla^2 \mathbf{u} \tag{2}$$

where $\mathbf{u}$ is velocity vector, ρ is the density, p is the pressure and μ is the dynamic viscosity. The blood was assumed to be Newtonian fluid with a constant density $\rho = 1060$ kg/m^3 and dynamic viscosity $\mu = 0.004$ Pa·s. A steady laminar flow model was used to simplify the problem and to reduce computation time. The no-slip boundary condition was applied at the aortic wall. A uniform velocity profile at the inlet of $U_{Inlet} = 0.5$ m/s was imposed in accordance with previous research [8]. A pressure-based solver was applied, and the SIMPLE algorithm was used for pressure-velocity coupling. For spatial discretization, the Least Squares Cell-based method was set for gradient calculations, the second-order method for pressure, and the second-order upwind method for momentum. The residuals were set to 10^{-5}.

The initial hybrid numerical mesh consisted of tetrahedral cells (with a typical cell size of 1 mm) in the interior and prismatic cells near the aortic wall (with a typical first layer thickness of 0.12 mm to properly capture velocity gradients). This mesh was converted to a

polyhedral numerical mesh to enhance numerical stability and convergence using Ansys Fluent 2021 R2 (Ansys, Canonsburg, Pennsylvania). A detailed numerical mesh dependency study is presented in Appendix C.

To improve computational efficiency for the 1000 CFD simulations, we performed parallel execution of 10 tasks with 100 cases per task on a DelftBlue supercomputer using 16 CPUs (Intel XEON E5-6248R, 3.0 GHz). The simulation runs for around 10 min for each case.

The resulting 3D fields of velocity, pressure, and wall shear stress were then interpolated onto the corresponding SSM meshes using ParaView. After interpolation, care was taken to eliminate potential non-zero velocity values along the aortic wall using an in-house code.

2.4. Neural networks

The Neural Networks (NNs) in this study are based on the structure proposed by Pajaziti et al. [24], which is a variant of Multilayer Perceptron (MLP). Initially, two separate neural networks are built and trained to predict velocity magnitude and direction. This is followed by additional NNs for pressure and wall shear stress, respectively. The training set consists of 900 cases, with the remaining 100 cases reserved for testing, which are unseen by the NNs. The input layer of the neural network is the deformation vector (also called the shape vector), with a dimension of 19, as illustrated in Fig. 3. The hidden layers are fully connected layers with Rectified linear units (ReLU) as the activation function. The width of the output layer is determined by the number of PCA modes required to capture 99% of the variance in pressure, velocity and WSS, as shown in the second column of Table 1. In the neural network, an inverse PCA operation is also incorporated to convert the obtained vector into real velocity, pressure, and WSS fields. The hidden layers' width (number of units), depth (number of layers), and learning rate are carefully tuned using the hyperparameter optimization framework Optuna [29]. The final hyperparameters are presented in Table D.3. For loss functions, we employ the mean absolute error (MAE) (Eq. (3)) for velocity magnitude, pressure, and WSS, while the cosine similarity (Eq. (4)) is used for velocity direction. These loss functions are calculated as follows:

$$\mathrm{MAE} = \frac{1}{N}\sum_{i=1}^{N}\left|Y(i) - \tilde{Y}(i)\right| \tag{3}$$

where $Y(i)$ represents the ground truth magnitude at node (i) obtained from CFD, $\tilde{Y}(i)$ is the predicted magnitude from the neural network, and N is the number of nodes in the volume mesh or surface mesh. The physical value of Y could be the velocity magnitude, pressure, or WSS magnitude. The cosine similarity is calculated as:

$$\mathrm{cosinesimilarity} \equiv cos\,(\theta) = -\frac{\vec{V}_{true}\cdot\vec{V}_{pred}}{\left|\vec{V}_{true}\right|\left|\vec{V}_{pred}\right|} \tag{4}$$

where $\vec{V}_{true}$ is the velocity-direction vector from the ground-truth (CFD), and $\vec{V}_{pred}$ is the velocity-direction vector predicted by the neural network. In the present study, we have $N = 34\,473$ for velocity magnitude and pressure, while $N = 5365$ is for WSS magnitude.

Notably, the neural networks sometimes fail to predict zero velocity values at the aortic wall. To address this, a no-slip condition layer was added to the neural networks, forcing the velocity on the wall (aorta surface) to be zero. The structure of the velocity neural networks (for both magnitude and direction) is shown in Fig. 3 as an example, where layer 'e' represents the no-slip condition layer.

To evaluate the accuracy of the neural networks outputs, two performance metrics proposed by Liang et al. [22] are adopted: (i) mean absolute error (MAE) (Eq. (3)) and, (ii) normalized mean absolute error (NMAE) (Eq. (5)). MAE directly reflects the absolute error between ground truth and prediction for individual cases. Since the ranges of ground truth vary from case to case, NMAE is also necessary to quantify the relative errors.

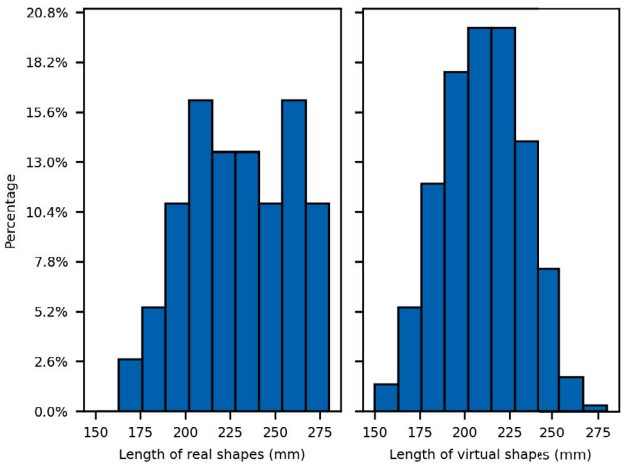

Fig. 4. Distribution of centerline lengths for 40 real shapes (left) and 1000 virtual shapes (right). Length range: 150–280 mm.

$$\mathrm{NMAE} = \frac{\mathrm{MAE}}{max(Y) - min(Y)} \times 100\% \tag{5}$$

where $max(Y)$ is the maximum magnitude, $min(Y)$ is the minimum magnitude of the ground-truth, and Y could represent velocity magnitude, pressure, or WSS.

2.5. Post-processing

In post-processing, we mainly focus on deriving WSS from the predicted velocity field. A new in-house code has been developed to calculate WSS through the following steps: (1) generate the gradient tensor of velocity vector $\nabla\vec{V}$, (2) extract the surface S of the domain, (3) generate the normal vector $\vec{N}_S$ of the surface, and lastly, (4) calculate the WSS $\vec{\tau}_w$ using the following equation:

$$\vec{\tau}_w = \mu\nabla\vec{V}\,\vec{N}_S \tag{6}$$

where $\vec{\tau}_w$ is the wall shear stress, μ is the viscosity of blood, $\vec{V}$ is the velocity field from neural networks, and $\vec{N}_S$ is the normal vector of the aortic wall surface.

3. Results

3.1. Statistical shape model of the aorta

In this study, in contrast to Pajaziti et al. [24], we did not clip geometries to maintain the same length, which makes the present scenario more realistic. The original geometry [25,26] was applied to obtain an anatomical structure. Due to the repeatability study on ten subjects, it is necessary to analyze the length characteristics of the real-shape dataset and virtual-shape dataset, which is related to the error and performance of neural networks. The centerline length distribution of the forty real geometries is given in Fig. 4. It can be seen that most of the geometries have a centerline length ranging from 200 to 275 mm, with only 7% of the shapes having a centerline length below 200 mm. The centerline length of the virtual shapes exhibits a Gaussian distribution ranging from 150 to 275 mm. Note that the centerline length of the real geometries does not show this Gaussian distribution due to the applied MRI-based scan/rescan method on a relatively small sample of ten subjects within a similar age group (26.5 ± 2.6), resulting in smaller geometrical variations.

Principal component analysis (PCA) was used to reduce the deformation matrix. The first 19 PCA modes capture 99% of the variance

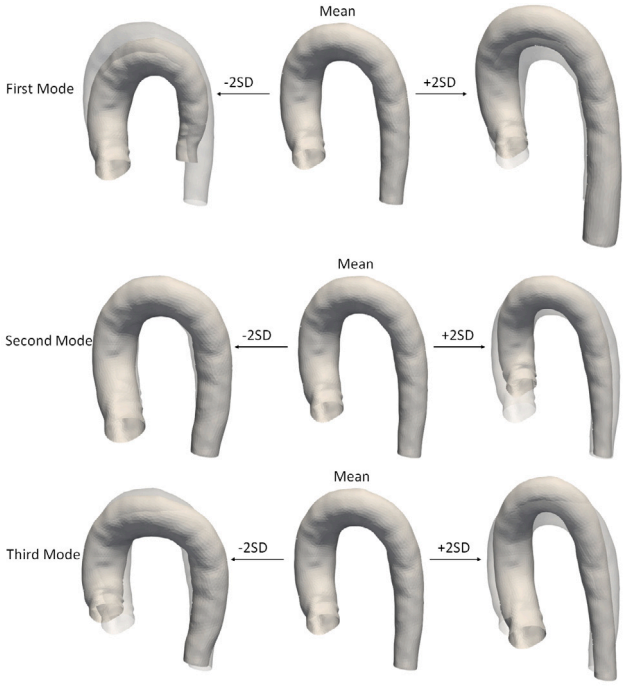

Fig. 5. Deformation of the mean aortic geometry when the first three modes change within ±2 standard deviations (SD).

in the original deformation matrix. The first, second, and third PCA modes capture 39%, 24%, and 15% of the variance, respectively (Fig. B.15). The resulting deformations of the mean aortic geometry when the leading three modes are changed within ±2 of standard deviation (SD) are shown in Fig. 5. Note that different PCA modes tend to describe different geometric features of aortas [24]. For example, when the initial geometrical set of the aortas is not clipped to the same length, their length is then controlled by series of PCA modes. When the first mode changes within ±2 standard deviation, both the length and diameter of the generated shape near the inlet and outlet change significantly. To quantify correlations between the PCA modes and virtually generated aortic shapes, we extracted the most salient geometrical features (i.e. diameter, length, tortuosity, torsion, and curvature) from 1000 virtual and compared them with the first three shape modes, Fig. 6. A correlation coefficient of 0.85 is obtained between the aortic length and the first PCA mode. This strong correlation is also evident in Fig. 5, where an increase of two standard deviations (2SD) in the first mode corresponds to an increase in aortic length. Significant correlations ($|R| > 0.7$) are also observed between the mean diameter and the second PCA mode, as well as between the aortic curvature and the first mode.

3.2. Neural networks predictions of 3D velocity and pressure

The scatter plot of predicted (NNs) versus the ground truth (CFD) velocity magnitude is shown in Fig. 7a. A good agreement is obtained (within ±10% for all cases). Note that the 100 cases shown here were not previously used in the training of NNs. The cosine similarity of velocity direction is −0.98 ± 0.01, as illustrated in Fig. 7b, confirming good accuracy. The Bland–Altman plot for velocity magnitude of the considered cases is presented in Fig. 8a. The Mean Absolute Error (MAE) of velocity-magnitude is 0.04 ± 0.01 m/s. The maximum and minimum MAE for velocity magnitude were found to be 0.08 m/s and 0.02 m/s, respectively. Based on the MAE of velocity-magnitude, the streamlines of best and worst cases are shown in Figs. 9(a) and 9(b), respectively. The Normalized Mean Absolute Error (NMAE) of velocity magnitude is 3.11 ± 1.15%, with maximum and minimum values of 7.41% and 1.30%, respectively. The NMAE of velocity magnitude in this study agrees well with the reported value of 3.99 ± 0.93% in [24].

The case-wise Bland–Altman plot for pressure is shown in Fig. 8b. The MAE of predicted pressure is 47.88±43.23 Pa, with maximum and minimum values of 284.17 Pa and 11.66 Pa, respectively. Based on the MAE of pressure, the best case and worst case are shown in Figs. 9(c) and 9(d), respectively. The NMAE of pressure is 4.48 ± 2.50%, with maximum and minimum values of 14.35% and 1.07%, respectively. The reported NMAE of pressure [24] is 6.01 ± 3.12%.

3.3. Derived and predicted wall shear stress

The first approach we tested in extracting WSS is based on a physics-informed method. In this approach, the derived WSS was calculated from the velocity field predicted by a neural network and compared with the WSS calculated from the ground truth CFD/SSM velocity field. Since the velocity gradient with boundary layer is difficult to capture during interpolation, the impact of interpolation will be discussed in Section 4.1. The MAE of derived WSS is 0.51 ± 0.21 Pa. The maximum and minimum MAE for derived WSS were found to be 1.50 Pa and 0.27 Pa, respectively. The NMAE of derived WSS is 4.8 ± 1.5%, with maximum and minimum values of 9.3% and 1.9%, respectively. The case-wise Bland–Altman plot for derived WSS is shown in Fig. 8c. Based on the MAE, the best and worst cases for derived WSS are shown in Figs. 10(a) and 10(b), respectively.

In the second approach, the WSS is obtained directly from the neural network (NN) for each shape. The MAE of predicted WSS is 1.04 ± 0.57 Pa, with maximum and minimum values of 4.51 Pa and 0.35 Pa, respectively. The case-wise Bland–Altman plot for predicted WSS is shown in Fig. 8d. Based on the MAE of predicted WSS, the best and worst cases are shown in Figs. 10(c) and 10(d), respectively. The NMAE of predicted WSS is 4.7 ± 2.0%, with maximum and minimum values of 10.8% and 0.9%, respectively.

3.4. Point and line analysis for best and worst cases

To comprehensively analyze the results of the best and worst cases, shown in Figs. 9 and 10, both point and line analyses were conducted. For the point analysis, 2000 nodes were randomly sampled from all the nodes of SSM meshes. The resulting node-wise Bland–Altman plots for pressure, velocity, derived WSS, and predicted WSS are presented in Fig. 11.

For the line analysis, cross-section averaged values along the centerlines were calculated for both the best case and worst cases. As shown in Fig. 12, for the best cases, the prediction values demonstrate excellent agreement with the ground-truth values. For the worst cases: (i) the prediction of velocity shows a significant deviation from the ground truth when $L/L_0 > 0.3$, (ii) the predictions of pressure, derived WSS, and predicted WSS show substantial deviations from the ground truth when $L/L_0 > 0.8$.

4. Discussion

4.1. Impact of interpolation and SSM mesh size

To assess the impact of interpolation and SSM mesh, we performed a CFD simulation of the mean aorta shape (see Fig. 5). We then interpolated the velocity and pressure fields onto three different SSM meshes: (i) a 2.0 mm size mesh, similar to the resolution of 4D Flow MRI [8], (ii) a mesh with 2.0 mm tetrahedral elements in the central part of the lumen and a 0.5 mm boundary layer prismatic mesh, and, (iii) a mesh with 2.0 mm tetrahedral elements in the central part of the lumen and a 0.4 mm boundary layer prismatic mesh. Our goal in refining the SSM mesh was to improve predictions of both the domain velocity field and the velocity gradient within relatively thin boundary

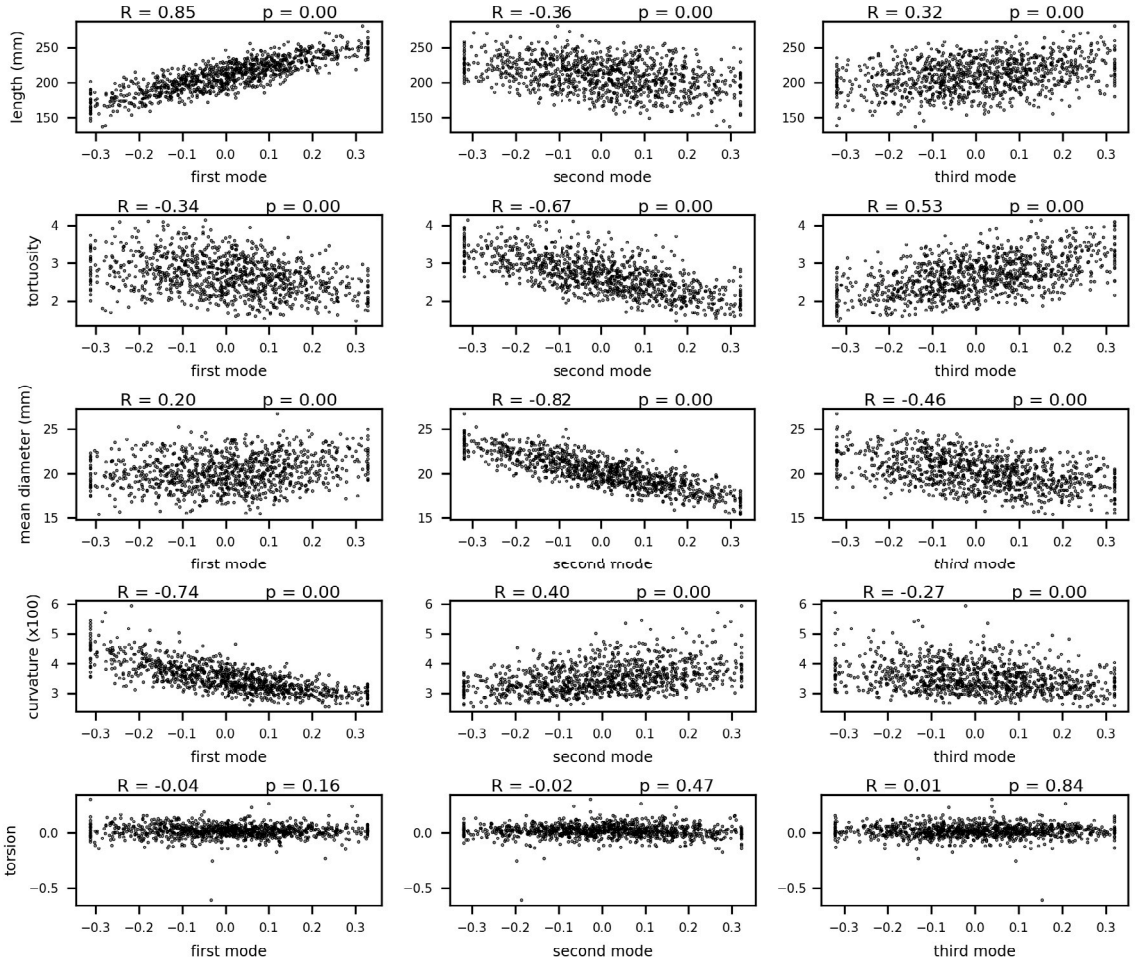

Fig. 6. Correlation between geometrical parameters and three PCA modes. Each row shows the relationship between geometrical features of aortas (length, tortuosity, diameter, curvature and torsion) and PCA modes.

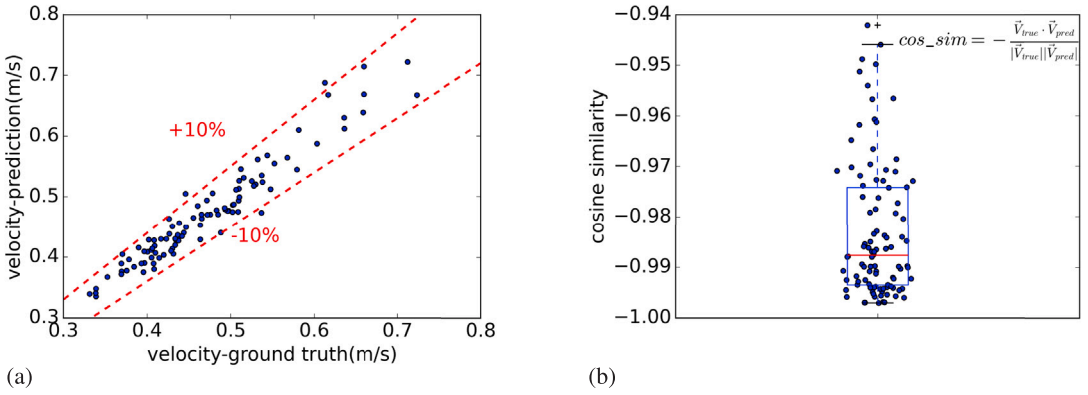

Fig. 7. (a) Predicted versus ground truth velocity magnitude. The dashed red lines show the boundaries with ±10% deviation. (b) The box plot of case-wise cosine similarity (targeted value = −1). All test case results (n = 100) are plotted.

layers. Fig. 13 illustrates the results of this analysis. The CFD mesh resulted in a maximum WSS value of approximately 15 Pa, which agrees well with ranges reported by Perinajová et al. [8].

After interpolating the velocity field onto the SSM meshes, the maximum values were: (i) approximately 4 Pa for the first mesh, (ii) 7.8 Pa for the second mesh, (iii) 9.2 Pa for the third mesh. These differences in maximum values are primarily due to mesh resolution. Moreover, the first and second meshes failed to accurately capture local WSS characteristics at the distal descending aorta, appearing blurred compared to CFD results. A key challenge in this process was managing small deviations (0.1 mm) between the CFD and SSM mesh surfaces at certain nodes. These deviations could lead to non-zero velocities on the wall after interpolation, necessitating manual correction to zero. This issue underscored the importance of using a finer boundary layer in

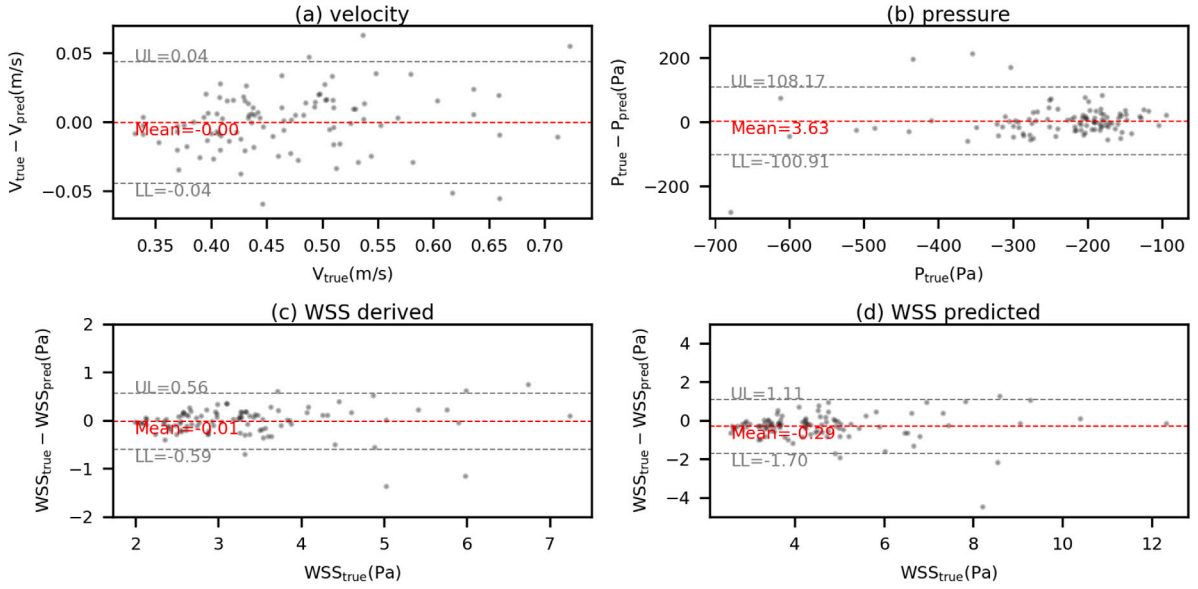

Fig. 8. Case-wise Bland–Altman plots for (a) velocity, (b) (relative) pressure, (c) WSS derived, (d) WSS predicted. True and predicted values are averaged for each case. Upper limit (UL) and lower limit (LL) represent the average difference ±1.96 standard deviations. All test cases (n = 100) are plotted.

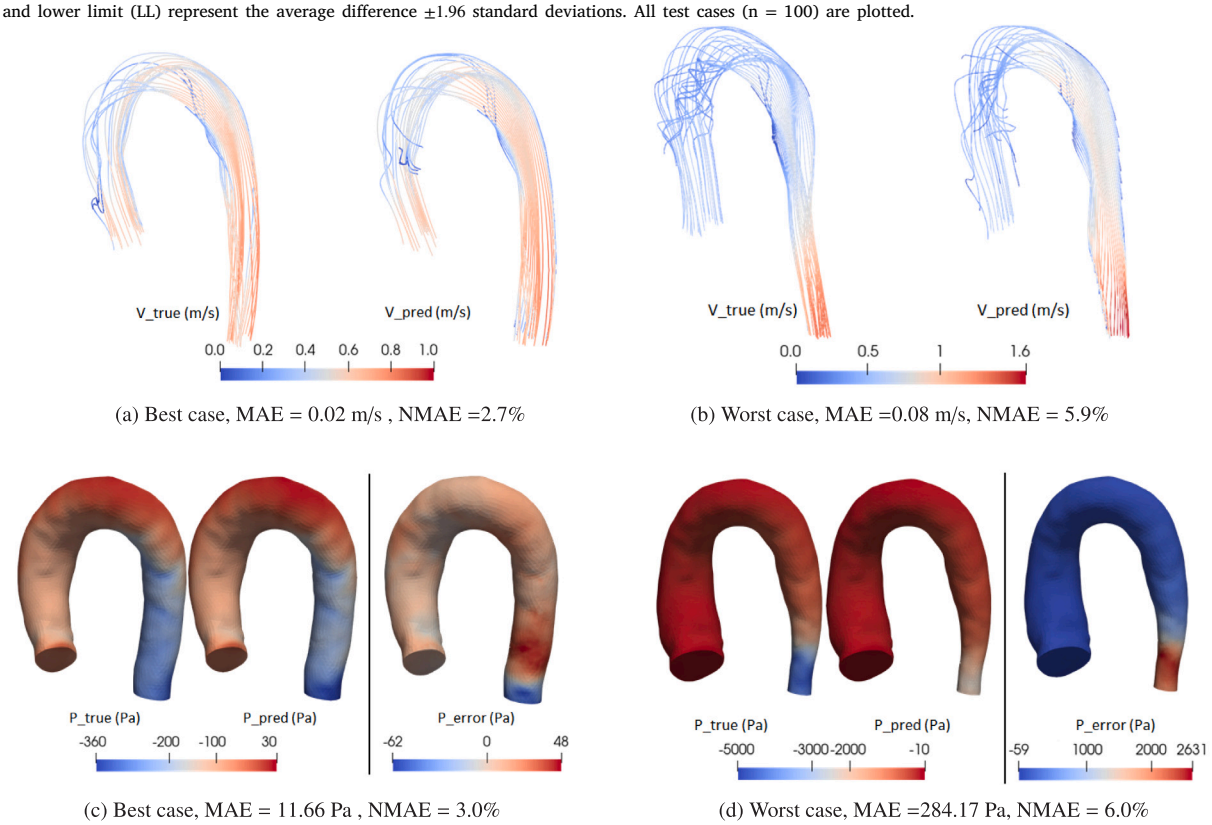

(a) Best case, MAE = 0.02 m/s , NMAE =2.7%

(b) Worst case, MAE =0.08 m/s, NMAE = 5.9%

(c) Best case, MAE = 11.66 Pa , NMAE = 3.0%

(d) Worst case, MAE =284.17 Pa, NMAE = 6.0%

Fig. 9. Neural network (NN) predictions for extreme cases (based on Mean Absolute Error (MAE)): streamlines colored by velocity magnitude (m/s): (a) best case, (b) worst case; (relative) pressure contours (Pa): (c) best case, (d) worst case. Note that P_error is the pressure difference between the predicted value and the true value.

the SSM mesh to prevent interpolation failures near the wall. Based on these findings, we selected the SSM mesh with 0.4 mm boundary layer for our study. This choice ensures consistent mesh correspondence across the neural networks dataset and provides a robust foundation for our subsequent analyses.

4.2. The performance of neural networks

The shape-driven neural networks applied in this study effectively predicted pressure, velocity, and WSS. The NMAE for these neural networks consistently ranged between 3% and 4%, aligning well with the values reported by Pajaziti et al. [24]. We believe this range represents the current performance limit of this neural network structure. Other deep neural network architectures, such as auto-encoders [22], can achieve lower NMAE values of 1.5% to 1.9%. However, these networks typically require significantly wider and deeper structures.

Our neural networks demonstrate compatibility with a wide range of GPUs, including older models. We successfully trained the networks without encountering memory issues on both the NVIDIA K4000 8 GB (2013) and A4500 20 GB (2021). Considering the trade-off between prediction accuracy and memory usage, our neural network achieves a good balance with acceptable error rates.

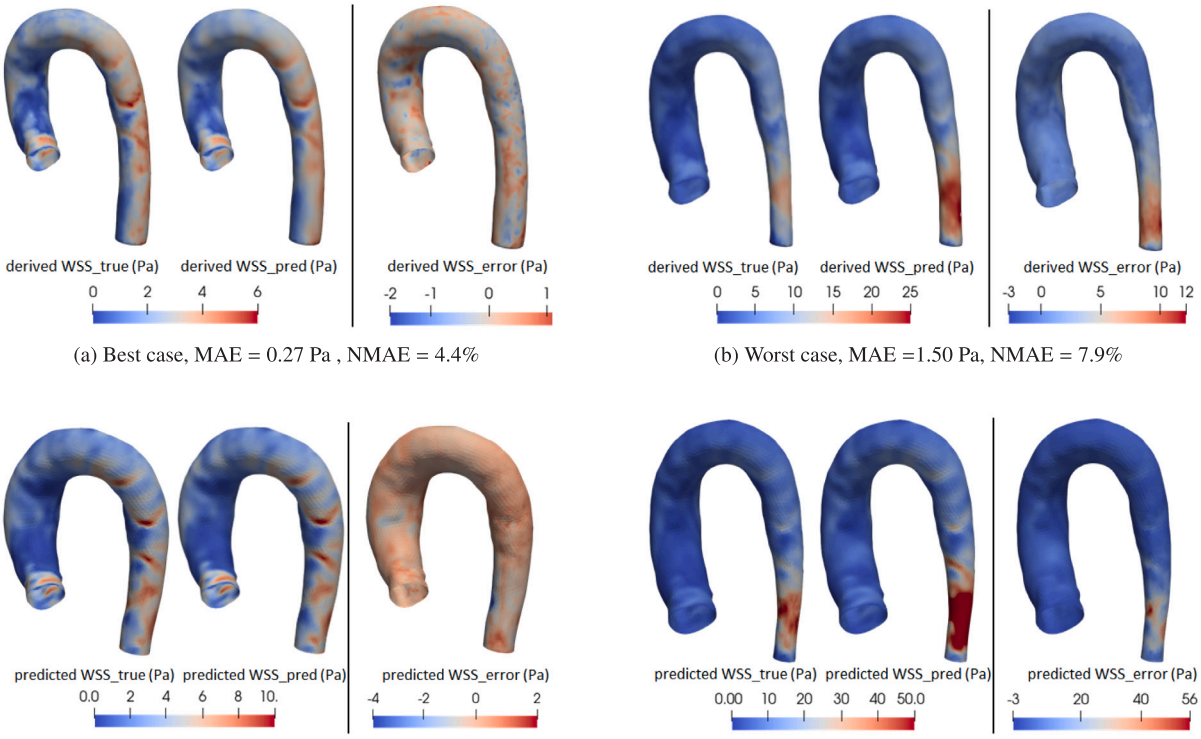

(a) Best case, MAE = 0.27 Pa , NMAE = 4.4%

(b) Worst case, MAE =1.50 Pa, NMAE = 7.9%

(c) Best case, MAE = 0.36 Pa , NMAE = 3.4%

(d) Worst case, MAE =4.51 Pa, NMAE = 8.4%

Fig. 10. The wall shear stress (WSS (Pa)) distribution for extreme cases based on Mean Absolute Error (MAE): derived WSS: (a) best case, (b) worst case, derived WSS_{error} equals derived ($WSS_{pred} - WSS_{true}$); predicted WSS: (c) best case, (d) worst case, predicted WSS_{error} equals predicted ($WSS_{pred} - WSS_{true}$).

Table 1
The MAE and NMAE caused by PCA for pressure, velocity and WSS.

	PCA mode	MAE	NMAE
Pressure	23	8.57 Pa	0.89%
Velocity	50	0.021 m/s	1.6%
WSS	35	0.51 Pa	2.2%

A key factor contributing to prediction errors in this study is the PCA layer within the neural networks, which reduces the dimensionality of the output fields. To quantify this effect, we performed a simple calculation using the following steps: (1) we applied PCA to the velocity magnitude matrix M, (2) we then used inverse PCA to reconstruct the velocity magnitude matrix $\bar{M}$, (3) we calculated the MAE and NMAE between M and $\bar{M}$. This analysis revealed that PCA introduces systematic errors with a mean MAE of 0.021 m/s and NMAE of 1.6%. These errors are inherent to the neural network structure and cannot be eliminated through training. Table 1 presents the systematic errors caused by PCA for analyzed quantities (i.e. pressure, velocity magnitude, and WSS).

4.3. Impact of geometry parameters

In this study, we correlated geometric parameters, rather than shape modes, with the MAE of pressure, velocity magnitude, and wall shear stress (WSS). These correlations are presented in Fig. E.17. The length and diameter of the aorta show significant correlations with the MAE of velocity magnitude, with diameter exhibiting the highest correlation ($R = -0.41$). As illustrated in Fig. 9(b), the MAE of velocity magnitude increases as the aorta's diameter decreases. Significant MAE of velocity magnitude typically occurs in aortas with smaller diameters. This is because velocity increases more sharply in narrow lumen compared to other zones, and the neural network struggles to accurately predict these large velocity magnitudes.

A similar relationship between geometry and MAE is observed for WSS prediction. Fig. E.17 shows that the MAE of WSS is statistically correlated with four geometric parameters: diameter, curvature, length, and tortuosity. Again, diameter demonstrates the highest correlation ($R = -0.34$). In Fig. 10(d), we observe higher MAE of WSS prediction in regions of the aorta with smaller diameters.

We also examined the relationship between geometry and the NMAE, as shown in Fig. E.18. Our analysis revealed varying influences of geometric parameters on NMAE: (1) for velocity magnitude NMAE: tortuosity shows the strongest correlation ($R = -0.34$), diameter also exhibits a significant correlation ($R = 0.29$), (2) for WSS NMAE: length, curvature, tortuosity, and torsion all exhibit significant correlations ($|R| > 0.2$), diameter does not show a significant correlation. Interestingly, while diameter significantly influences the MAE on both velocity magnitude and WSS (as discussed earlier), its impact on NMAE varies between these two parameters.

Our analysis reveals that geometric parameters which induce significant variations in the flow field characteristics are more likely to result in higher prediction errors by the neural networks. Specifically, features such as narrow diameters, high tortuosity, and extreme curvatures tend to create complex flow patterns that challenge the predictive accuracy of our models.

4.4. Comparison of derived WSS and predicted WSS

When choosing between physics-informed and neural network (NN)-based methods for Wall Shear Stress (WSS) prediction, both training cost and accuracy must be considered. The physics-informed method for WSS calculation involves a more complex workflow: (1) interpolating the velocity field onto an SSM mesh with a boundary layer to capture near-wall velocity gradients, (2) training two neural

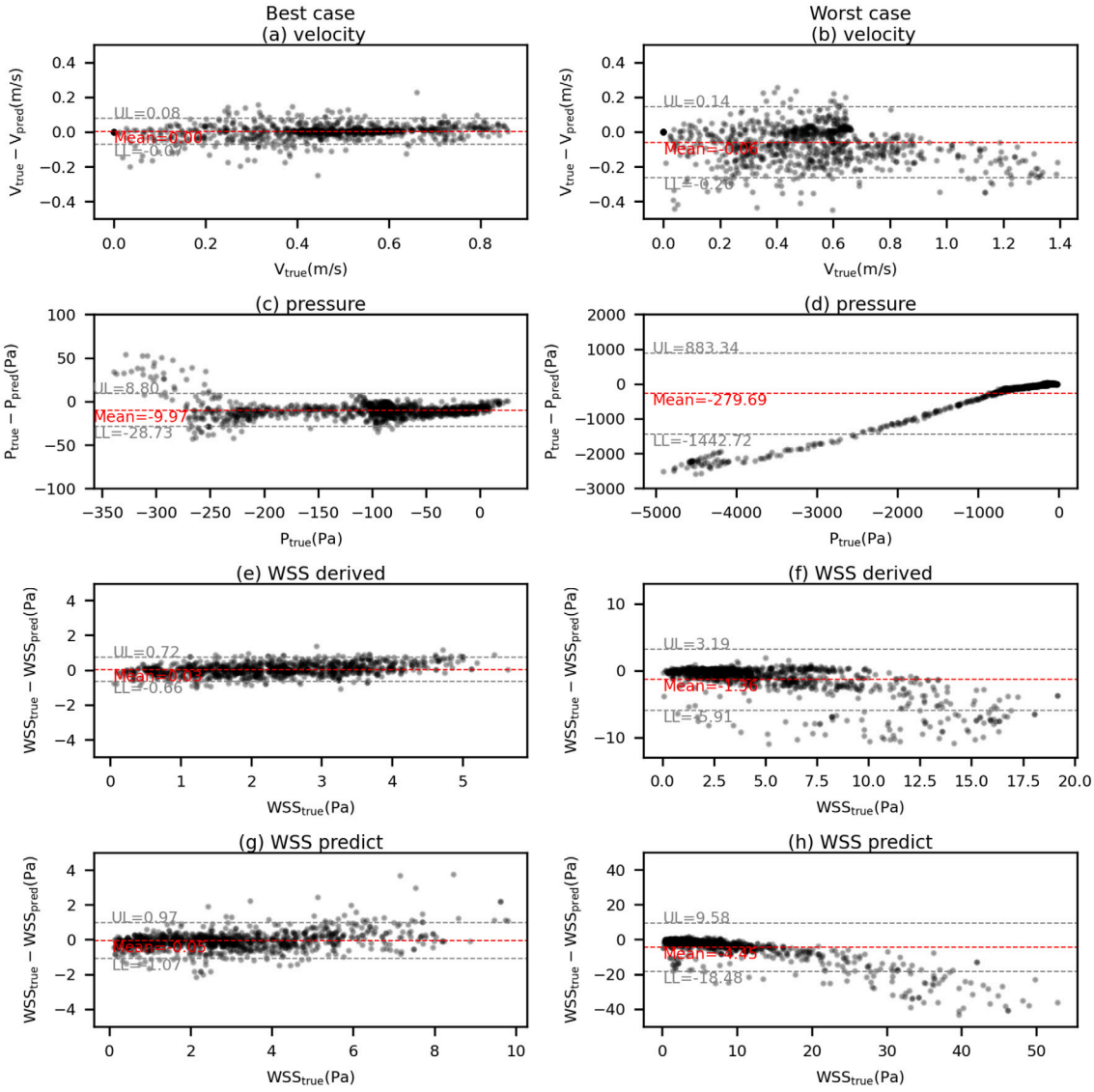

Fig. 11. Node-wise Bland–Altman plots for best and worst cases: velocity (a–b), (relative) pressure (c–d), derived WSS (e–f), predicted WSS (g–h). True and predicted values based on all nodes (N): pressure and velocity N = 34,473, and WSS N = 5365. Upper limit (UL) and lower limit (LL) represent the average difference ± 1.96 standard deviations, which are calculated using all nodes. For clarity, 2000 randomly sampled nodes are plotted.

networks to predict velocity fields, (3) applying a series of post-processing steps to derive WSS. This approach is significantly more time-consuming than the direct NN-based method. In terms of performance, both methods can predict the distribution characteristics of WSS. However, the physics-informed approach struggles to capture absolute WSS values accurately. Despite adding a prism layer to the SSM meshes, some loss of velocity gradient information occurs. This loss is compounded when neural networks predict velocity fields, introducing errors at multiple stages and causing the final WSS predictions to deviate from CFD results.

The choice between these two methods depends on the specific research objectives: (1) if the primary goal is WSS prediction, the NN-based method is more accurate and efficient in capturing both absolute values and distribution characteristics of WSS, (2) if the focus is on predicting patient-specific velocity fields, the physics-informed method can adequately predict velocity fields while generating WSS as a byproduct with acceptable accuracy. In conclusion, researchers should carefully consider their primary objectives and available computational resources when selecting between these two approaches for WSS prediction.

4.5. Limitation of present work

Several limitations of the current work should be addressed. Addressing these limitations in future work will be crucial for improving the model's accuracy and applicability to a wider range of clinical scenarios.

4.5.1. Limited dataset

Due to the lack of a large patient-specific MRI dataset, we utilized a small dataset of 40 real shapes, which only included healthy aortas. In contrast to other studies [24], future work should incorporate Thoracic Aortic Aneurysm (TAA) and Coarctation of the Aorta (COA) cases. Moreover, the 40 real shapes were derived from scans and rescans of only 10 volunteers, resulting in geometric similarities among the samples. Future efforts will focus on collecting a more diverse, high-quality medical image dataset.

4.5.2. Simplified CFD modeling

To expedite simulations, several simplifying assumptions were made in the CFD modeling: (1) only laminar flow was considered, neglecting

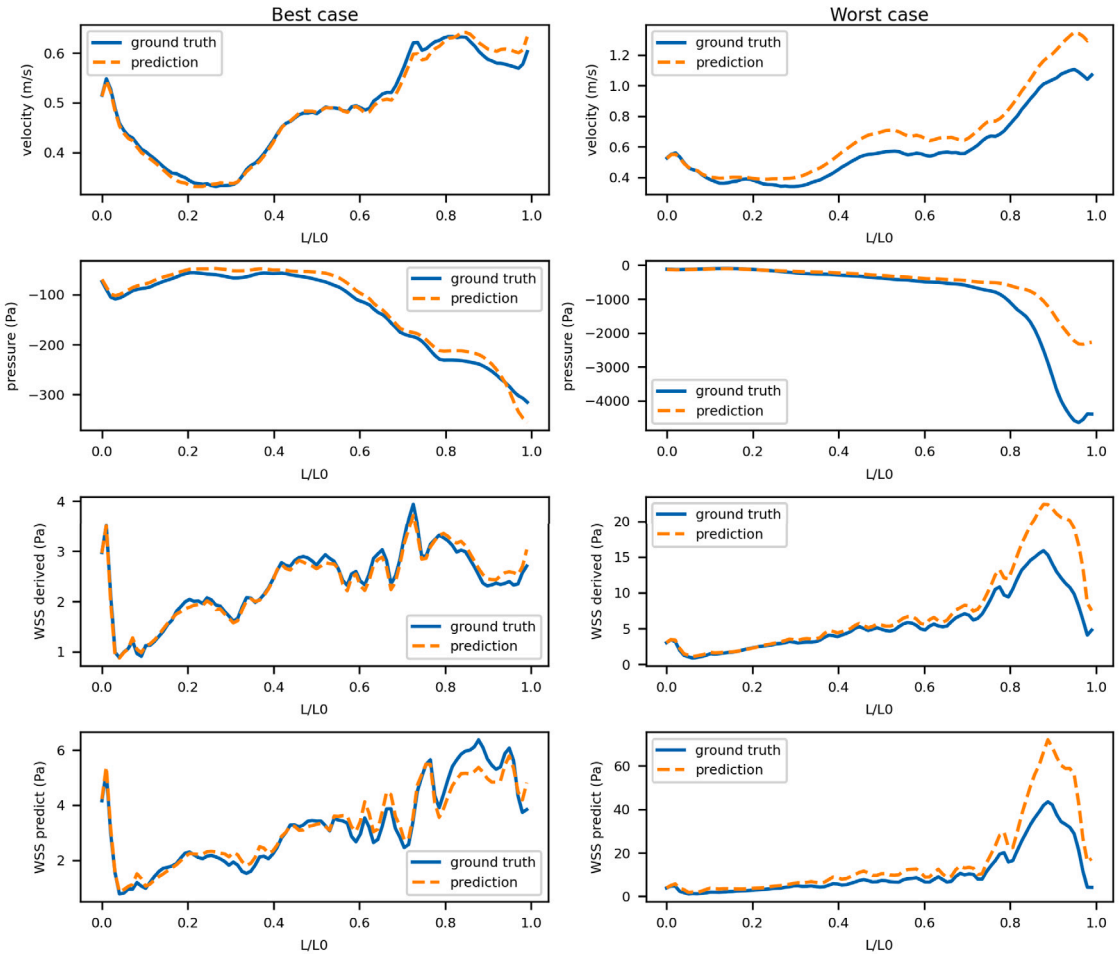

Fig. 12. Cross-section averaged values along centerlines for best (-left) and worst cases (-right): velocity, (relative) pressure, derived WSS, predicted WSS, respectively. L/L0 represents the normalized distance along the centerline.

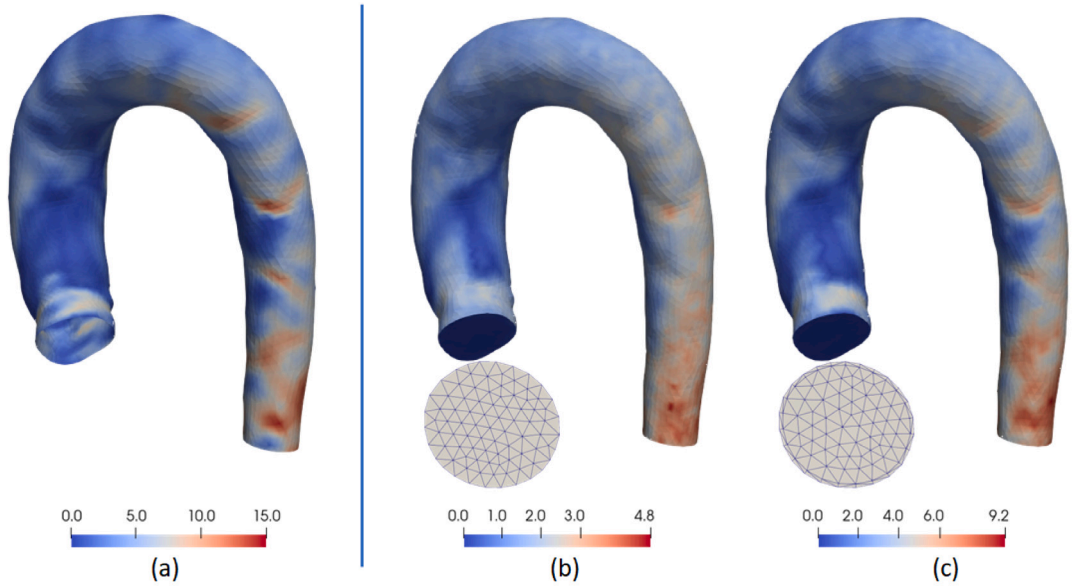

Fig. 13. Impact of mesh interpolation on wall shear stress (WSS (Pa)) calculation for the mean aortic shape: (a) original CFD solution velocity field, (b) velocity interpolated into 2 mm tetrahedral mesh, (c) velocity interpolated onto 2 mm tetrahedral mesh with 0.4 mm prism layer. Note: WSS (Pa) calculated from each velocity field to assess interpolation impact.

potential turbulence, (2) geometries were simplified to include only one inlet and one outlet, (3) movement of the aortic wall was neglected, (4) a fixed velocity was defined at the inlet, rather than treating it as a

dependent parameter in the neural networks. These simplifications may limit the model's applicability to more complex, real-world scenarios.

4.5.3. Data processing limitations

The CFD dataset was not directly fed into the neural networks. Instead, the process involved: (1) interpolating the CFD dataset (velocity, pressure, and wall shear stress) onto an SSM mesh, (2) compressing the interpolated data into a vector using Principal Component Analysis (PCA). This approach introduces potential errors during both the data interpolation and compression stages, which may affect the overall accuracy of the neural network predictions.

5. Conclusions

We developed shape-driven neural networks to predict 3D pressure, velocity field, and wall shear stress in aortic flow. We found that the trained neural networks can simultaneously predict flow fields (velocity, pressure, and WSS) within seconds. This is significantly faster than traditional CFD methods that typically require 10 or more minutes. The mean absolute error (MAE) of velocity predictions is 0.04 ± 0.01 m/s, with a normalized MAE of $3.11 \pm 1.15\%$, agreeing well with previously reported values in the literature. For wall shear stress, the MAE is 1.04 ± 0.57 Pa, with a normalized MAE of $4.7 \pm 2.0\%$. The accurate prediction of wall shear stress is due to the prism layer in the statistical shape model (SSM) meshes and the no-slip boundary layer implemented in the neural networks. This approach allows wall shear stress to be derived from the predicted velocity field as a byproduct with acceptable accuracy. Errors in prediction are primarily due to interpolation between CFD and SSM meshes. In contrast, for neural network predicted wall shear stress, the workflow is significantly simpler, and the predicted values are in close agreement with the derived WSS approach. For projects specifically focused on wall shear stress estimations, our neural network-based method is recommended for its ease of use and accuracy.

List of abbreviations

ADAM	Adaptive Moment Estimation optimizer
CFD	Computational Fluid Dynamics
DNN	Deep Neural Network
GCI	Grid Convergence Index
LDDMM	Large Deformation Diffeomorphic Metric Mapping
MAE	Mean Absolute Error
ML	Machine Learning
NMAE	Normalized Mean Absolute Error
PCA	Principal Component Analysis
SSM	Statistical Shape Model
VMTK	Vascular Modeling Toolkit
WSS	Wall Shear Stress

CRediT authorship contribution statement

Daiqi Lin: Writing – review & editing, Writing – original draft, Software, Methodology, Investigation. **Saša Kenjereš:** Writing – review & editing, Writing – original draft, Supervision, Resources, Funding acquisition, Conceptualization.

Declaration of competing interest

None declared.

Acknowledgments

The research of Daiqi Lin was made possible by the financial support of the Chinese Scholarship Council (CSC). The authors acknowledge the use of computational resources of the DelftBlue supercomputer, provided by Delft High Performance Computing Centre (https://www.tudelft.nl/dhpc).

Table C.2
The Grid Convergence Index (GCI) estimation for the aorta of mean shape. f1, f2, f3 refer to the pressure or velocity for the coarse, medium and fine mesh, respectively. r is the grid refinement ratio. p is the order of convergence, $f_{h=0}$ is the Richardson extrapolation estimate, $GCI_{1,2}$ is the GCI for the coarse and medium mesh, and $GCI_{2,3}$ is the GCI for the medium and fine mesh.

	Pressure	Velocity
f1	−153.67 Pa	0.592 m/s
f2	−166.35 Pa	0.580 m/s
f3	−168.52 Pa	0.573 m/s
r	1.23	1.23
p	8.68	3.05
$f_{h=0}$	−168.97 Pa	0.565 m/s
$GCI_{1,2}$	1.9×10^{-2}	3.1×10^{-2}
$GCI_{2,3}$	3.3×10^{-3}	1.7×10^{-2}
Asymptotic	1.01	0.99

Appendix A. Aorta geometries

The real aorta geometries used in the present work, shown in Fig. A.14, are based on our previous studies [8,25].

Appendix B. PCA modes and variance

To reduce the size of the deformation matrix $\mathcal{M}[40,450]$, Principle Component Analysis (PCA) was applied. The first three modes capture 39%, 24%, and 15% of the variance (total 78%), respectively. The first 19 modes are capturing 99.1% of the variance, as shown in Fig. B.15.

Appendix C. Mesh dependency

The mesh dependence analysis was performed to assess the accuracy of the simulations. Three different meshes were generated for the computational domain of the mean shape: (1) coarse: 1.57 million cells; (2) medium: 2.59 million cells; (3) fine: 4.76 million cells. The pressure and velocity along the centerline were compared for the three meshes. As shown in Fig. C.16, the medium mesh with 2.59 million cells is fine enough to capture mesh-independent flow features. Table C.2 shows the grid convergence index (GCI) estimation for the three meshes.

Appendix D. Hyperparameters in neural networks

The neural networks in this study are based on the Multilayer Perceptron (MLP). The basic structure of neural networks is shown in Fig. 3, in which 'a' is the input layer of MLP, 'b' is the hidden layer of MLP, 'c' is the output layer of MLP, 'd' is the inverse Principal Component Analysis (PCA) layer, and 'e' is the no-slip condition layer. The hyperparameters used in the final neural networks are shown in Table D.3.

Appendix E. The correlation between geometry parameters and errors

In order to explore the relationship between geometry and errors, five geometrical parameters (diameter, length, tortuosity, torsion, and curvature) are correlated with MAE (Fig. E.17) and NMAE (Fig. E.18). The Pearson correlation coefficients are shown at the top of each figure. The first rows of Figs. E.17 and E.18 show the correlation between pressure errors and the five geometrical parameters. The correlations for velocity and WSS are shown in the second rows and third rows, respectively. A comprehensive discussion of these results is presented in Section 4.3.

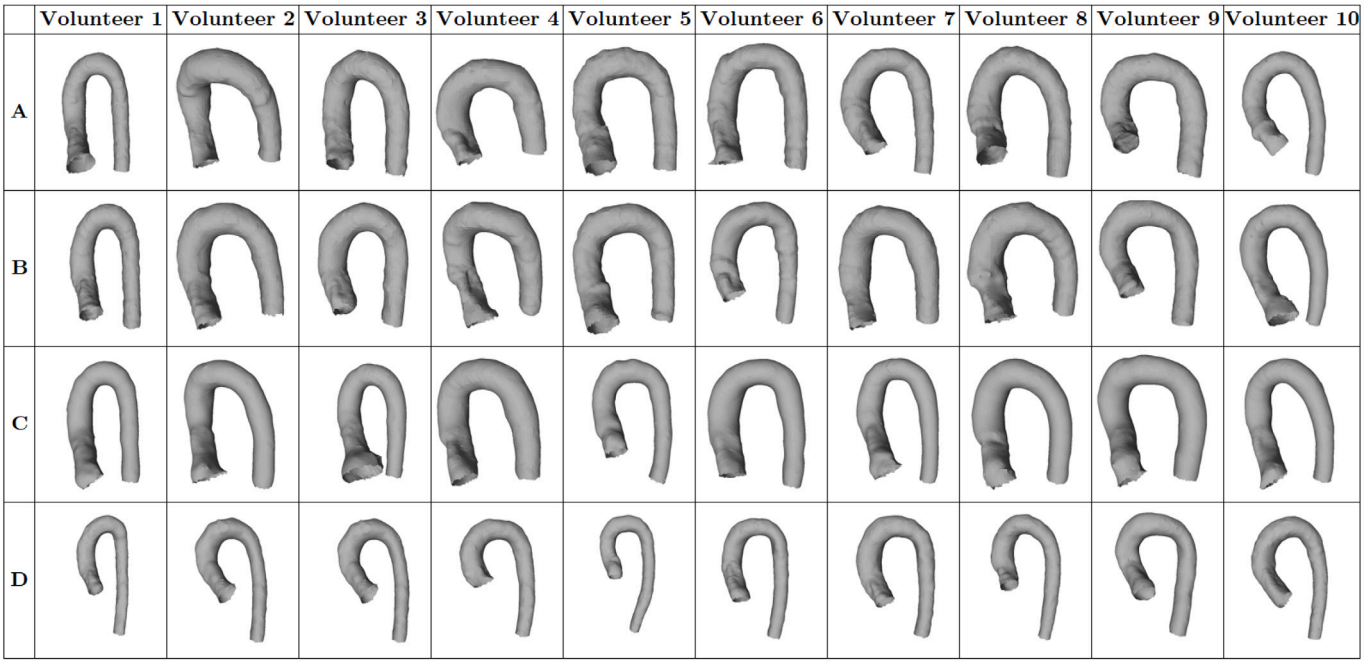

Fig. A.14. Overview of forty aortic geometries obtained from 4D Flow MRI: ten subjects, each with four different segmentation approaches, as addressed in [8,25].

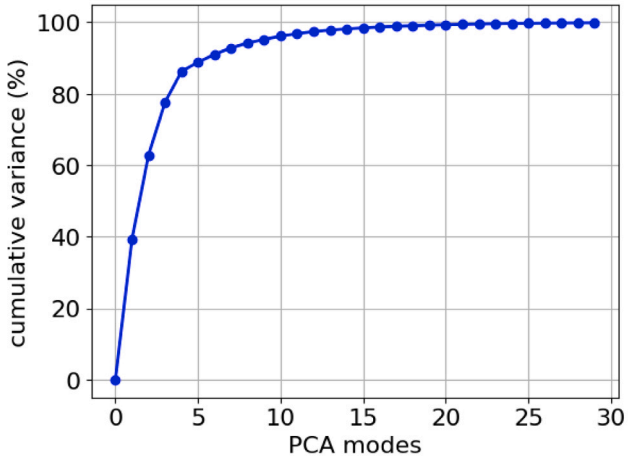

Fig. B.15. Cumulative variance (in %) captured by the PCA modes.

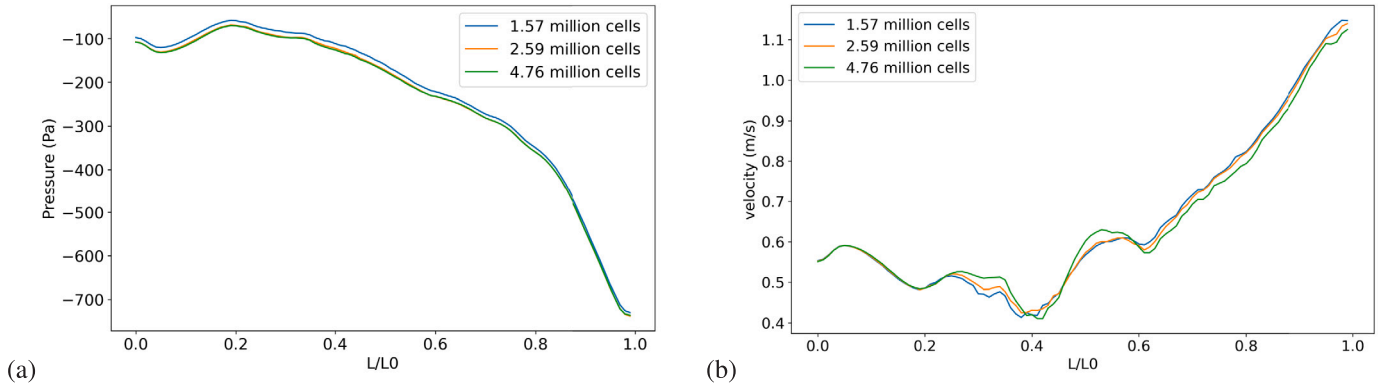

Fig. C.16. Mesh dependence analysis along the centerline of the mean aortic shape: (a) (relative) pressure profile, (b) velocity magnitude profile. Note that $L/L0$ represents the normalized distance along the aortic centerline (from inlet to outlet).

Table D.3
The hyperparameters in generated neural networks for pressure, velocity magnitude, velocity direction, and wall shear stress, respectively. The size of the layer refers to the number of neurons in each layer, and the number of layers indicates how many layers are in the neural networks. Layer 'd' and layer 'c' are lambda functions without neurons, so for these two layers, only the output shapes are mentioned in the table.

Neural network	Pressure	Velocity-magnitude	Velocity-direction	WSS
Size of layer 'a'	19	19	19	19
Size of layer 'b'	550	400	200	500
Number of layer 'b'	5	4	4	5
Size of layer 'c'	23	50	50	35
Output shape of layer 'd'	34 473	34 473	(34473, 3)	5365
Output shape of layer 'e'	None	34 473	(34473, 3)	None
Learning rate	1.2×10^{-5}	3.0×10^{-4}	2.9×10^{-3}	2.3×10^{-3}
Batch size	30	30	30	30
Loss function	MAE	MAE	Cosine similarity	MAE
Optimizer	ADAM	ADAM	ADAM	ADAM

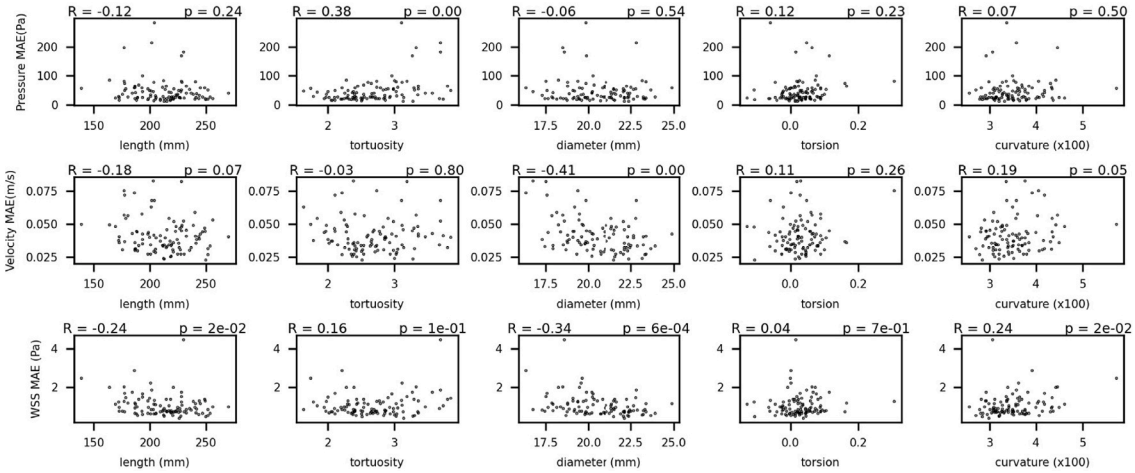

Fig. E.17. Correlation between geometrical parameters and Mean Absolute Error (MAE) for pressure, velocity, and WSS. Pearson correlation coefficients are displayed above each plot.

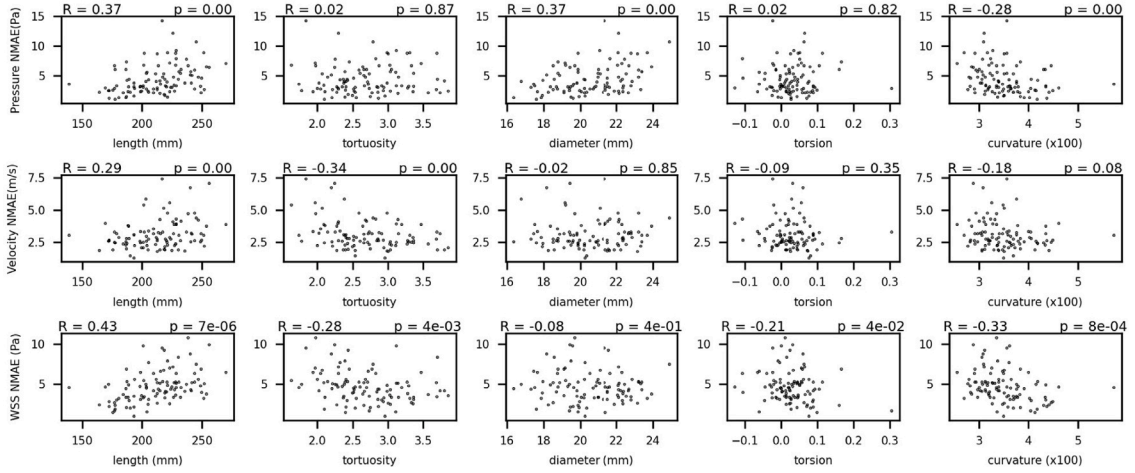

Fig. E.18. Correlation between geometrical parameters and Normalized Mean Absolute Error (NMAE) for pressure, velocity, and WSS. Pearson correlation coefficients are displayed above each plot.

References

[1] C.J. François, M. Markl, M.L. Schiebler, E. Niespodzany, B.R. Landgraf, C. Schlensak, A. Frydrychowicz, Four-dimensional, flow-sensitive magnetic resonance imaging of blood flow patterns in thoracic aortic dissections, J. Thorac. Cardiovasc. Surg. 145 (5) (2013) 1359–1366.

[2] M. Cibis, W.V. Potters, F.J. Gijsen, H. Marquering, P. Van Ooij, E. VanBavel, J.J. Wentzel, A.J. Nederveen, The effect of spatial and temporal resolution of cine phase contrast MRI on wall shear stress and oscillatory shear index assessment, PLoS One 11 (9) (2016) e0163316.

[3] M.J.F.G. Ramaekers, B.P. Adriaans, J.F. Juffermans, H.C. Van Assen, S.C.A.M. Bekkers, A.J.H.A. Scholte, S. Kenjereš, H.J. Lamb, J.E. Wildberger, J.J.M. Westenberg, S. Schalla, Characterization of ascending aortic flow in patients with degenerative aneurysms: a 4D flow magnetic resonance study, Invest. Radiol. 56 (2021) 494–500.

[4] B. Stemkens, E.S. Paulson, R.H. Tijssen, Nuts and bolts of 4D-MRI for radiotherapy, Phys. Med. Biol. 63 (21) (2018) 21TR01.

[5] S.A. Goldstein, A. Evangelista, S. Abbara, et al., Multimodality imaging of diseases of the thoracic aorta in adults: From the American society of echocardiography and the European association of cardiovascular imaging: Endorsed by the society of cardiovascular computed tomography and society for cardiovascular

magnetic resonance, J. Am. Soc. Echocardiogr. 28 (2015) 119–182.
[6] S. Boccalini, X. Gao, P.H. Kitslaar, R.P.J. Budde, S. Tu, B.P.F. Lelievedlt, J. Dijkstra, J.H.C. Reiber, A novel software tool for semi-automatic quantification of thoracic aorta dilatation on baseline and follow-up computed tomography angiograph, Int. J. Cardiovasc. Imaging 35 (2019) 711–723.
[7] R. Perinajová, J.F. Juffermans, J.L. Mercado, J.-P. Aben, L. Ledoux, J.J.M. Westenberg, H.J. Lamb, S. Kenjereš, Assessment of turbulent blood flow and wall shear stress in aortic coarctation using image-based simulations, Biomed. Eng. Online 20 (1) (2021) 84.
[8] R. Perinajová, J.F. Juffermans, J.J.M. Westenberg, R.L.F. van der Palen, P.J. van den Boogaard, H.J. Lamb, S. Kenjereš, Geometrically induced wall shear stress variability in CFD-MRI coupled simulations of blood flow in the thoracic aortas, Comput. Biol. Med. 133 (2021) 104385.
[9] M.J.F.G. Ramaekers, I.B. van der Vlugt, J.J.M. Westenberg, R. Perinajová, H.J. Lamb, J.E. Wildeberger, S. Kenjereš, S. Schalla, Flow patterns in ascending aortic aneurysms: Determining the role of hypertension using phase contrast magnetic resonance and computational fluid dynamics, Comput. Biol. Med. 172 (2024) 108310.
[10] S. Kenjereš, On recent progress in modelling and simulations of multi-scale transfer of mass, momentum and particles in bio-medical applications, Flow, Turbul. Combust. 96 (2016) 837–860.
[11] J. Fujisue, Y. Takayama, S. Tonoki, H. Tanaka, Utility of computational fluid dynamics for prediction of efficacy of the surgical interventions for aortic coarctation in adults, JTCVS Tech. 18 (2023) 16–21.
[12] E.L. Schwarz, L. Pegolotti, M.R. Pfaller, A.L. Marsden, Beyond CFD: Emerging methodologies for predictive simulation in cardiovascular health and disease, Biophys. Rev. 4 (1) (2023).
[13] P.A. Yushkevich, G. Gerig, ITK-SNAP: an intractive medical image segmentation tool to meet the need for expert-guided segmentation of complex medical images, IEEE Pulse 8 (4) (2017) 54–57.
[14] R. Kikinis, S.D. Pieper, K.G. Vosburgh, 3D slicer: a platform for subject-specific image analysis, visualization, and clinical support, in: Intraoperative Imaging and Image-Guided Therapy, Springer, 2013, pp. 277–289.
[15] L. Antiga, M. Piccinelli, L. Botti, B. Ene-Iordache, A. Remuzzi, D.A. Steinman, An image-based modeling framework for patient-specific computational hemodynamics, Med. Biol. Eng. Comput. 46 (2008) 1097–1112.
[16] I. Wolf, M. Vetter, I. Wegner, M. Nolden, T. Bottger, M. Hastenteufel, M. Schobinger, T. Kunert, H.-P. Meinzer, The medical imaging interaction toolkit (MITK): a toolkit facilitating the creation of interactive software by extending VTK and ITK, in: Medical Imaging 2004: Visualization, Image-Guided Procedures, and Display, Vol. 5367, SPIE, 2004, pp. 16–27.
[17] A. Updegrove, N.M. Wilson, J. Merkow, H. Lan, A.L. Marsden, S.C. Shadden, SimVascular: an open source pipeline for cardiovascular simulation, Ann. Biomed. Eng. 45 (2017) 525–541.
[18] H. Jasak, OpenFOAM: Open source CFD in research and industry, Int. J. Nav. Archit. Ocean. Eng. 1 (2) (2009) 89–94.
[19] N.M. Wilson, A.K. Ortiz, A.B. Johnson, The vascular model repository: a public resource of medical imaging data and blood flow simulation results, J. Med. Dev. 7 (4) (2013) 040923.
[20] C.G. Fonseca, M. Backhaus, D.A. Bluemke, R.D. Britten, J.D. Chung, B.R. Cowan, I.D. Dinov, J.P. Finn, P.J. Hunter, A.H. Kadish, The Cardiac Atlas Project—an imaging database for computational modeling and statistical atlases of the heart, Bioinformatics 27 (16) (2011) 2288–2295.
[21] A. Taebi, Deep learning for computational hemodynamics: A brief review of recent advances, Fluids 7 (6) (2022).
[22] L. Liang, W. Mao, W. Sun, A feasibility study of deep learning for predicting hemodynamics of human thoracic aorta, 2019/12/07, J. Biomech. 99 (2020) 109544.
[23] M. Morgan, A.R. Murali, G. Preston, Y.A. Sima, L.A.M. Chamorro, C. Bourantas, R. Torii, A. Mathur, A. Baumbach, M.C. Jacob, S. Karabasov, R. Krams, A physics-based machine learning technique rapidly reconstructs the wall-shear stress and pressure fields in coronary arteries, Front. Cardiovasc. Med. 10 (2023) 1–12.
[24] E. Pajaziti, J. Montalt-Tordera, C. Capelli, R. Sivera, E. Sauvage, M. Quail, S. Schievano, V. Muthurangu, Shape-driven deep neural networks for fast acquisition of aortic 3D pressure and velocity flow fields, PLoS Comput. Biol. 19 (4) (2023) e1011055.
[25] R.L.F. van der Palen, A.A.W. Roest, P.J. van den Boogaard, A. de Roos, N.A. Blom, J.J.M. Westenberg, Scan–rescan reproducibility of segmental aortic wall shear stress as assessed by phase-specific segmentation with 4D flow MRI in healthy volunteers, Magn. Reson. Mater. Phys. Biol. Med. 31 (2018) 653–663.
[26] J.F. Juffermans, J.J.M. Westenberg, P.J. van den Boogaard, A.A.W. Roest, H.C. van Assen, R.L.F. van der Palen, H.J. Lamb, Reproducibility of aorta segmentation on 4D flow MRI in healthy volunteers, J. Magn. Reson. Imaging 53 (4) (2021) 1268–1279.
[27] A. Bône, M. Louis, B. Martin, S. Durrleman, Deformetrica 4: an open-source software for statistical shape analysis, in: Shape in Medical Imaging: International Workshop, ShapeMI 2018, Held in Conjunction with MICCAI 2018, Granada, Spain, September 20, 2018, Proceedings, Springer, 2018, pp. 3–13.
[28] M.F. Beg, M.I. Miller, A. Trouvé, L. Younes, Computing large deformation metric mappings via geodesic flows of diffeomorphisms, Int. J. Comput. Vis. 61 (2005) 139–157.
[29] T. Akiba, S. Sano, T. Yanase, T. Ohta, M. Koyama, Optuna: A next-generation hyperparameter optimization framework, in: Proceedings of the 25th ACM SIGKDD International Conference on Knowledge Discovery and Data Mining, 2019.

Update

Computers in Biology and Medicine

Volume 192, Issue PA, June 2025, Page

DOI: https://doi.org/10.1016/j.compbiomed.2025.110330

Computers in Biology and Medicine 192 (2025) 110330

Contents lists available at ScienceDirect

Computers in Biology and Medicine

journal homepage: www.elsevier.com/locate/compbiomed

Corrigendum to "Towards fast and reliable estimations of 3D pressure, velocity and wall shear stress in aortic blood flow: CFD-based machine learning approach" [Comput. Biol. Med. 191 (2025) 110137]

Daiqi Lin [a,b], Saša Kenjereš [a,b,*]

[a] Department of Chemical Engineering, Faculty of Applied Sciences, Delft University of Technology, Van der Maasweg 9, 2629 HZ, Delft, the Netherlands
[b] J.M. Burgerscentrum Research School for Fluid Mechanics, Mekelweg 2, 2628 CD, Delft, the Netherlands

<Note to JM: Errors in article heads, particularly titles, author names, affiliations must not be repeated. In such cases, use the correct title, authors, affiliation(s), etc. If the corrigendum is the result of authorship changes, include the correct author details in the article head.>

The authors regret that the final version of the Graphical Abstract was not included with the original manuscript submission. The Graphical Abstract is now available.

We apologize for any inconvenience this may have caused.

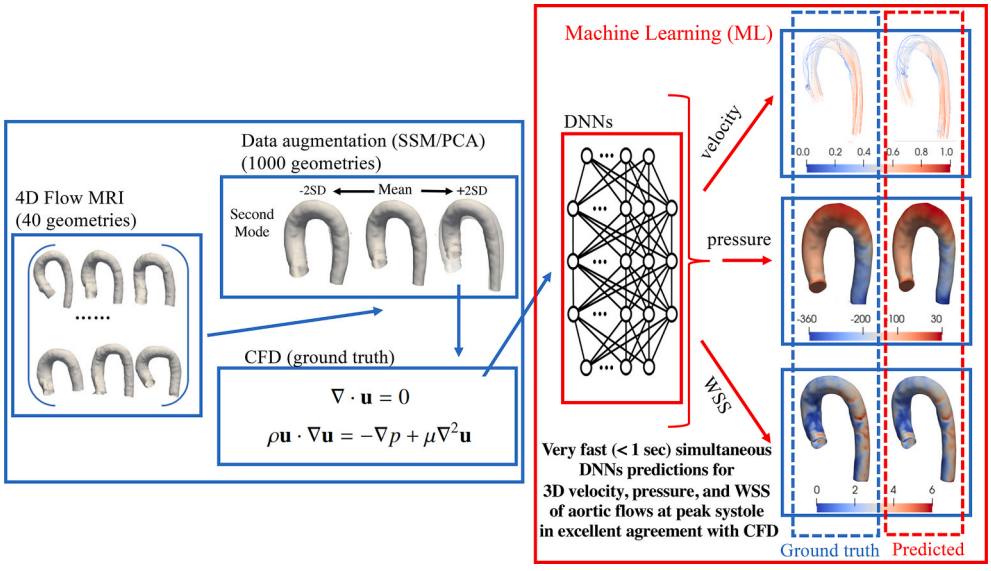

DOI of original article: https://doi.org/10.1016/j.compbiomed.2025.110137.
* Corresponding author. at: Department of Chemical Engineering, Faculty of Applied Sciences, Delft University of Technology, Van der Maasweg 9, 2629 HZ, Delft, the Netherlands.
E-mail addresses: d.l.lin@tudelft.nl (D. Lin), s.kenjeres@tudelft.nl (S. Kenjereš).

https://doi.org/10.1016/j.compbiomed.2025.110330

Available online 9 May 2025